

## NONLINEAR GENERALIZED BEAM THEORY FOR COLD-FORMED STEEL MEMBERS

N. SILVESTRE and D. CAMOTIM\*

*Civil Engineering Department, IST, Technical University of Lisbon,  
Av. Rovisco Pais, 1049-001 Lisbon, Portugal*

*\*dcamotim@civil.ist.utl.pt*

Received 5 March 2003

Accepted 6 August 2003

A geometrically nonlinear Generalized Beam Theory (GBT) is formulated and its application leads to a system of equilibrium equations which are valid in the large deformation range but still retain and take advantage of the unique GBT mode decomposition feature. The proposed GBT formulation, for the elastic post-buckling analysis of isotropic thin-walled members, is able to handle various types of loading and arbitrary initial geometrical imperfections and, in particular, it can be used to perform “exact” or “approximate” (i.e., including only a few deformation modes) analyses. Concerning the solution of the system of GBT nonlinear equilibrium equations, the finite element method (FEM) constitutes the most efficient and versatile numerical technique and, thus, a beam FE is specifically developed for this purpose. The FEM implementation of the GBT post-buckling formulation is reported in some detail and then employed to obtain numerical results, which validate and illustrate the application and capabilities of the theory.

*Keywords:* Nonlinear generalized beam theory; transverse extension modes; shear modes; post-buckling analysis; thin-walled isotropic members.

### 1. Introduction

In order to assess the structural efficiency of slender thin-walled members (e.g., cold-formed steel profiles), it is necessary to obtain in-depth information about their global (flexural and flexural-torsional — see Fig. 1(a)) and local (local-plate and distortional — see Figs. 1(b) and (c)) buckling and post-buckling behaviors. This task involves (i) identifying the relevant buckling modes, (ii) calculating the associated bifurcation stresses and (iii) determining the corresponding post-buckling equilibrium paths and strength values, which must account for the presence of unavoidable initial imperfections. Besides contributing to a better understanding of geometrically nonlinear behavior of members, all the above information also plays a crucial role in the development, validation and calibration of design rules and methodologies. Indeed, only reliable and physically-based models lead to rational, fully efficient and easy-to-use formulae and/or procedures.

The advances in the field of computational mechanics during the last few decades, together with the continuous and fast growing availability of powerful

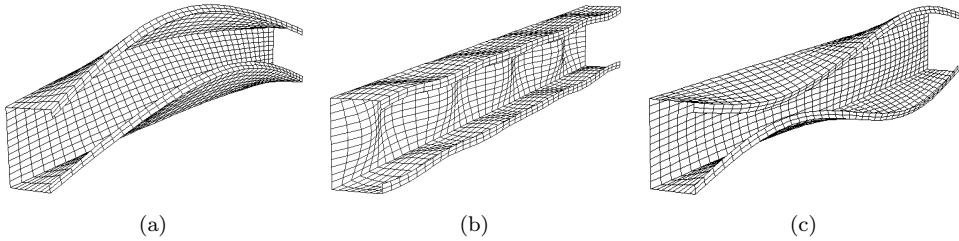


Fig. 1. Member (a) flexural-torsional (b) local-plate and (c) distortional buckling.

computational tools (hardware and software), have led to a widespread and routine use of numerical structural analyses. Among the methods employed, the finite element method<sup>1–3</sup> (FEM) is, by far, the most popular, mostly because of its (i) versatility, (ii) solid mathematical foundations and (iii) large dissemination. In the case of slender thin-walled members, the type and number (mesh) of finite elements adopted must enable the adequate modelling of various local and global instability phenomena. This requirement often leads to the adoption of a large number of complex geometrically nonlinear shell elements to discretize the member.<sup>4</sup>

Since the FEM geometrically nonlinear analyses of slender thin-walled members invariably (i) involve fine FE meshes and (ii) require computer-intensive incremental-iterative numerical techniques, they cannot be used for routine design applications (even with the present-day fast computers). In order to overcome this limitation, one can use the finite strip method<sup>5–9</sup> (FSM), which has already been shown to provide a very efficient alternative to FEM linear stability analyses (for prismatic members). In the last decade, the Generalized Beam Theory<sup>10,11</sup> (GBT) has also emerged as another competitive (and conceptually different) alternative to FEM linear stability analyses (again for prismatic members). Finally, one should also mention the “spline finite strip method”<sup>6</sup> (SFSM), that somewhat combines FSM and FEM. In this method, the longitudinal variation of the displacement field is approximated by “B<sub>3</sub>-spline functions”, instead of analytical expressions. The SFSM can be used in a much wider range of problems than the FSM, namely to perform buckling<sup>12</sup> and post-buckling (geometrically nonlinear) analyses<sup>13,14</sup> of members with support conditions other than pinned and free-to-warp end sections. In the context of buckling analyses, “bubble functions” have been used to improve the SFSM efficiency<sup>15</sup> (here the accuracy is achieved with less strips).

At present, the “exact” geometrically nonlinear behavior of thin-walled members can only be accurately determined by resorting to FE<sup>16–19</sup> or SFS<sup>13,14,20–25</sup> analyses. In particular, assessing the local-global mode interaction phenomena still constitutes a formidable task, mostly due to the need to model short and long-wave structural behaviors simultaneously. In addition, the results yielded by the above numerical analyses are often difficult to process and/or interpret, a feature that often clouds the full understanding of all phenomena under consideration.

GBT was developed by Schardt<sup>10,11</sup> in the mid-1980s and later employed extensively by Davies and co-workers,<sup>26,27</sup> mostly to analyze the linear stability behavior

of cold-formed steel members. It accounts for both cross-section (local) and member (global) deformations and has been shown to be a very efficient tool for analyzing local and global stability behavior of thin-walled cold-formed steel (isotropic) and composite (orthotropic) members.<sup>28,29</sup> In fact, by decomposing the member buckling modes into linear combinations of “pure deformation modes”, GBT offers possibilities not available even through the use of powerful numerical techniques (e.g., the FEM or the FSM) and provides a general and elegant approach to obtain accurate solutions for several stability problems. Indeed, since the GBT d.o.f. are *modal* (instead of *nodal*) displacements, all the member deformed configuration “ingredients” are revealed by the analysis, which still retains the accuracy of the “conventional” methods. In addition, this feature also enables the derivation of analytical formulae to evaluate local and global buckling loads.<sup>30</sup> However, since the available GBT equations are only valid for small deformations and moderate rotations, significant developments and extensions are required before genuine post-buckling analyses can be performed.<sup>4</sup>

The objective of this paper is to present the derivation of a nonlinear isotropic GBT, which extends the available theory into the post-buckling range, thus making it possible to perform geometrically nonlinear analyses in open section thin-walled members made of cold-formed steel profiles. The application of this nonlinear theory leads to a system of equilibrium equations which are valid in the large deformation range but still retain and take advantage of the unique GBT mode decomposition feature. Moreover, it is possible (i) to consider different types of loading, (ii) to take into account the presence of arbitrary initial geometrical imperfections and (iii) to determine, with great accuracy, “exact” and “approximate” (i.e., including just a few deformation modes) member post-buckling equilibrium paths.

Initially, the principle of virtual work is used to derive the nonlinear equilibrium equations governing the geometrically nonlinear behavior (large displacement) of isotropic elastic thin-walled members displaying open cross-sections. These equations involve three local displacement components, defined on the member mid-surface and having the longitudinal variation described by a single function. Next, the paper focuses on the set of operations and procedures required to obtain the cross-section deformation modes and determine the corresponding modal mechanical properties. It is worth noting that this task is considerably more complex than the corresponding one performed in the “traditional” GBT,<sup>11,26</sup> due to the need to account for two additional sets of deformation modes: (i) shear and (ii) transverse extension modes.<sup>31</sup> Then, the paper describes the steps involved in the formulation and numerical implementation of a nonlinear beam FE specifically developed to solve the GBT system of nonlinear equilibrium equations and boundary conditions. It should be remarked that, since no path-following numerical technique to handle branch-switching at bifurcation points was implemented, all the post-buckling analyses dealt with in this work correspond to *initially imperfect* members. In order to validate and illustrate the application and capabilities of the nonlinear GBT, several numerical results, concerning the geometrically nonlinear (post-buckling) behaviour of uniformly compressed plates and lipped channel and Z-section

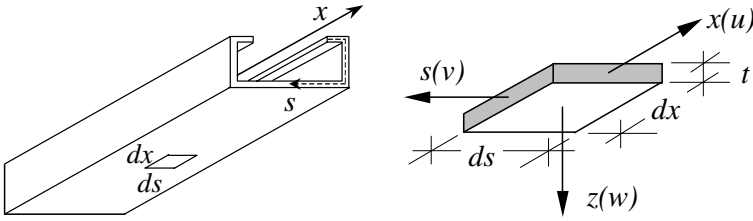


Fig. 2. Coordinate system and displacement components.

columns, are presented and discussed. Some of these results are compared with values obtained from finite element and finite strip analyses and the computational efficiency of the proposed GBT-based approach is also addressed. It is mostly due to the possibility of performing “*approximate analyses*”, i.e., analyses that account for only a few selected GBT deformation modes.

## 2. Derivation of GBT Post-Buckling Equations

Consider a thin-walled prismatic member with an arbitrary open cross-section formed by  $n$  walls (plate elements). The coordinate system and displacement components are defined as depicted in Fig. 2.  $x$ ,  $s$  and  $z$  are the coordinates along the member length, cross-section mid-line and wall thickness, while  $u$ ,  $v$  and  $w$  are the associated displacement components. The member cross-section is assumed to be discretized into  $n + 1$  natural nodes (corresponding to the wall longitudinal edges or “fold-lines”) and  $m$  intermediate nodes (in general, at least one per wall).

In order to reach a displacement representation compatible with the classical beam theory, the components  $u(x, s)$ ,  $v(x, s)$ ,  $w(x, s)$  are expressed as

$$u(x, s) = u_k(s)\phi_{k,x}(x) \quad v(x, s) = v_k(s)\phi_k(x) \quad w(x, s) = w_k(s)\phi_k(x), \quad (1)$$

where  $(\cdot)_{,x} \equiv d(\cdot)/dx$ , the functions  $u_k(s)$ ,  $v_k(s)$  and  $w_k(s)$  represent the variation of  $u$ ,  $v$  and  $w$  along the cross-section mid-line and  $\phi(x)$  is a “displacement amplitude function” defined along the member length  $L$ . Moreover, one may also include member initial geometric imperfections in the form

$$\bar{u}(x, s) = u_k(s)\bar{\phi}_{k,x}(x) \quad \bar{v}(x, s) = v_k(s)\bar{\phi}_k(x) \quad \bar{w}(x, s) = w_k(s)\bar{\phi}_k(x), \quad (2)$$

where  $\bar{\phi}$  and  $\phi$  have similar meanings. The relevant nonlinear strain-displacement relations employed are

$$\begin{aligned} \varepsilon_{xx} &= u_{,x} + \frac{1}{2}(v_{,x}^2 + w_{,x}^2) - zw_{,xx} - \bar{u}_{,x} - \frac{1}{2}(\bar{v}_{,x}^2 + \bar{w}_{,x}^2) + z\bar{w}_{,xx} \\ \varepsilon_{ss} &= v_{,s} + \frac{1}{2}(v_{,s}^2 + w_{,s}^2) - zw_{,ss} - \bar{v}_{,s} - \frac{1}{2}(\bar{v}_{,s}^2 + \bar{w}_{,s}^2) + z\bar{w}_{,ss} \\ \gamma_{xs} &= u_{,s} + v_{,x} + v_{,x}v_{,s} + w_{,x}w_{,s} - 2zw_{,xs} - \bar{u}_{,s} - \bar{v}_{,x} \\ &\quad - \bar{v}_{,x}\bar{v}_{,s} - \bar{w}_{,x}\bar{w}_{,s} + 2z\bar{w}_{,xs} \end{aligned} \quad (3)$$

or, after taking into account Eqs. (1) and (2),

$$\begin{aligned}
 \varepsilon_{xx} &= u_k \phi_{k,xx} + \frac{1}{2}(v_k v_i + w_k w_i) \phi_{k,x} \phi_{i,x} - z w_k \phi_{k,xx} \\
 &\quad - u_k \bar{\phi}_{k,xx} - \frac{1}{2}(v_k v_i + w_k w_i) \bar{\phi}_{k,x} \bar{\phi}_{i,x} + z w_k \bar{\phi}_{k,xx} \\
 \varepsilon_{ss} &= v_{k,s} \phi_k + \frac{1}{2}(v_{k,s} v_{i,s} + w_{k,s} w_{i,s}) \phi_k \phi_i - z w_{k,ss} \phi_k \\
 &\quad - v_{k,s} \bar{\phi}_k + \frac{1}{2}(v_{k,s} v_{i,s} + w_{k,s} w_{i,s}) \bar{\phi}_k \bar{\phi}_i - z w_{k,ss} \bar{\phi}_k \\
 \gamma_{xs} &= (u_{k,s} + v_k) \phi_{k,x} + (v_k v_{i,s} + w_k w_{i,s}) \phi_{k,x} \phi_i - 2z w_{k,s} \phi_{k,x} \\
 &\quad - (u_{k,s} + v_k) \bar{\phi}_{k,x} - (v_k v_{i,s} + w_k w_{i,s}) \bar{\phi}_{k,x} \bar{\phi}_i + 2z w_{k,s} \bar{\phi}_{k,x}. \tag{4}
 \end{aligned}$$

Since the thin-walled member is isotropic and elastic material, the constitutive relation of each wall element is defined by

$$\begin{Bmatrix} \sigma_{xx} \\ \sigma_{ss} \\ \sigma_{xs} \end{Bmatrix} = \begin{bmatrix} Q_{11} & Q_{12} & 0 \\ Q_{12} & Q_{22} & 0 \\ 0 & 0 & Q_{66} \end{bmatrix} \begin{Bmatrix} \varepsilon_{xx} \\ \varepsilon_{ss} \\ \gamma_{xs} \end{Bmatrix} = \frac{E}{1-\nu^2} \begin{bmatrix} 1 & \nu & 0 \\ \nu & 1 & 0 \\ 0 & 0 & \frac{1}{2}(1-\nu) \end{bmatrix} \begin{Bmatrix} \varepsilon_{xx} \\ \varepsilon_{ss} \\ \gamma_{xs} \end{Bmatrix}, \tag{5}$$

where  $E$  and  $\nu$  are Young’s modulus and Poisson’s ratio, respectively.

### 2.1. Variation of the strain energy

The variation of the member strain energy is given by

$$\delta U = \int_{\Omega_V} \sigma_{ij} \delta \varepsilon_{ij} dV = \delta U_1 + \delta U_2 + \delta U_3 - \delta \bar{U}_1 - \delta \bar{U}_2 - \delta \bar{U}_3, \tag{6}$$

where  $\Omega_V$  is the volume of  $n$  plates forming the member and the bar ( $\bar{\quad}$ ) identifies a term stemming from the initial imperfections. By incorporating Eqs. (4) and (5) into (6) and integrating over the cross-section (coordinates  $s, z$ ), one obtains the following expressions for  $\delta U$  terms

$$\begin{aligned}
 \delta U_1 &= \int_L (C_{kh} \phi_{k,xx} \delta \phi_{h,xx} + B_{kh} \phi_k \delta \phi_h + D_{kh}^I \phi_{k,x} \delta \phi_{h,x} \\
 &\quad + D_{kh}^{II} \phi_k \delta \phi_{h,xx} + D_{hk}^{II} \phi_{k,xx} \delta \phi_h) dx \\
 \delta U_2 &= \int_L \left( C_{kjh} \phi_{k,xx} \phi_{j,x} \delta \phi_{h,x} + \frac{1}{2} C_{hjk} \phi_{k,x} \phi_{j,x} \delta \phi_{h,xx} \right. \\
 &\quad + \left( B_{kjh} + \frac{1}{2} B_{hjk} \right) \phi_k \phi_j \delta \phi_h + D_{kjh}^I \phi_{k,x} \phi_{j,x} \delta \phi_h \\
 &\quad + (D_{hkj}^I + D_{khj}^I) \phi_{k,x} \phi_j \delta \phi_{h,x} + \frac{1}{2} D_{hjk}^{II} \phi_k \phi_j \delta \phi_{h,xx} \\
 &\quad \left. + D_{kjh}^{II} \phi_{k,xx} \phi_j \delta \phi_h + D_{kjh}^{III} \phi_k \phi_{j,x} \delta \phi_{h,x} + \frac{1}{2} D_{hjk}^{III} \phi_{k,x} \phi_{j,x} \delta \phi_h \right) dx
 \end{aligned}$$

$$\begin{aligned} \delta U_3 = & \int_L \left( \frac{1}{2} C_{kijh} \phi_{k,x} \phi_{i,x} \phi_{j,x} \delta \phi_{h,x} + \frac{1}{2} B_{kijh} \phi_k \phi_i \phi_j \delta \phi_h \right. \\ & + D_{kijh}^I \phi_{k,x} \phi_i \phi_j \delta \phi_{h,x} + D_{kihj}^I \phi_{k,x} \phi_i \phi_j \delta \phi_h \\ & \left. + \frac{1}{2} D_{kijh}^{II} \phi_{k,x} \phi_{i,x} \phi_j \delta \phi_h + \frac{1}{2} D_{jhki}^{II} \phi_k \phi_i \phi_{j,x} \delta \phi_{h,x} \right) dx. \end{aligned} \tag{7}$$

$$\begin{aligned} \delta \bar{U}_1 = & \int_L (C_{kh} \bar{\phi}_{k,xx} \delta \phi_{h,xx} + B_{kh} \bar{\phi}_k \delta \phi_h + D_{kh} \bar{\phi}_{k,x} \delta \phi_{h,x} \\ & + D_{kh}^{II} \bar{\phi}_k \delta \phi_{h,xx} + D_{hk}^{II} \bar{\phi}_{k,xx} \delta \phi_h) dx \\ \delta \bar{U}_2 = & \int_L \left( C_{kjh} \bar{\phi}_{k,xx} \bar{\phi}_{j,x} \delta \phi_{h,x} + \frac{1}{2} C_{hjk} \bar{\phi}_{k,x} \bar{\phi}_{j,x} \delta \phi_{h,xx} + B_{kjh} \bar{\phi}_k \bar{\phi}_j \delta \phi_h \right. \\ & + \frac{1}{2} B_{hjk} \bar{\phi}_k \bar{\phi}_j \delta \phi_h + D_{kjh}^I \bar{\phi}_{k,x} \bar{\phi}_{j,x} \delta \phi_h + D_{khj}^I \bar{\phi}_{k,x} \bar{\phi}_j \delta \phi_{h,x} \\ & + D_{hkj}^I \bar{\phi}_k \bar{\phi}_j \delta \phi_{h,x} + D_{kjh}^{II} \bar{\phi}_{k,xx} \bar{\phi}_j \delta \phi_h + \frac{1}{2} D_{hjk}^{II} \bar{\phi}_k \bar{\phi}_j \delta \phi_{h,xx} \\ & \left. + D_{kjh}^{III} \bar{\phi}_k \bar{\phi}_{j,x} \delta \phi_{h,x} + \frac{1}{2} D_{hjk}^{III} \bar{\phi}_{k,x} \bar{\phi}_{j,x} \delta \phi_h \right) dx \\ \delta \bar{U}_3 = & \int_L \left( \frac{1}{2} C_{kijh} \bar{\phi}_{k,x} \bar{\phi}_{i,x} \phi_{j,x} \delta \phi_{h,x} + \frac{1}{2} B_{kijh} \bar{\phi}_k \bar{\phi}_i \phi_j \delta \phi_h \right. \\ & + D_{kijh}^I \bar{\phi}_{k,x} \bar{\phi}_i \phi_j \delta \phi_{h,x} + D_{kihj}^I \bar{\phi}_{k,x} \bar{\phi}_i \phi_{j,x} \delta \phi_h \\ & \left. + \frac{1}{2} D_{kijh}^{II} \bar{\phi}_{k,x} \bar{\phi}_{i,x} \phi_j \delta \phi_h + \frac{1}{2} D_{jhki}^{II} \bar{\phi}_k \bar{\phi}_i \phi_{j,x} \delta \phi_{h,x} \right) dx, \end{aligned} \tag{8}$$

where  $\delta U_1$ ,  $\delta U_2$  and  $\delta U_3$  are linear, quadratic and cubic functionals of the mode amplitude functions  $\phi_i$ ;  $\delta \bar{U}_1$  and  $\delta \bar{U}_3$  are linear and quadratic functionals of the imperfection amplitude functions  $\bar{\phi}_i$ ; and  $\delta \bar{U}_2$  has linear and quadratic terms in  $\bar{\phi}_i$ . The second, third and fourth order tensors appearing in Eqs. (7) and (8), which stem from the cross-section integration of products involving  $u_k(s)$ ,  $w_k(s)$ ,  $w_k(s)$  and their derivatives, are defined by

$$\begin{aligned} C_{kh} &= \int_b (A_{11} u_k u_h + D_{11} w_k w_h) ds \\ B_{kh} &= \int_b (A_{22} v_{k,s} v_{h,s} + D_{22} w_{k,ss} w_{h,ss}) ds \\ D_{kh}^I &= \int_b [A_{66} (v_k + u_{k,s})(v_h + u_{h,s}) + 4D_{66} w_{k,s} w_{h,s}] ds \\ D_{kh}^{II} &= \int_b (A_{12} v_{k,s} u_h + D_{12} w_{k,ss} w_h) ds \end{aligned}$$

$$\begin{aligned}
 C_{kjh} &= \int_b A_{11} u_k (v_j v_h + w_j w_h) ds \\
 B_{kjh} &= \int_b A_{22} v_{k,s} w_{j,s} w_{h,s} ds \\
 D_{kjh}^I &= \int_b A_{66} (v_k + u_{k,s}) w_j w_{h,s} ds \\
 D_{kjh}^{II} &= \int_b A_{12} u_k w_{j,s} w_{h,s} ds \\
 D_{kjh}^{III} &= \int_b A_{12} v_{k,s} (v_j v_h + w_j w_h) ds \\
 C_{kijh} &= \int_b A_{11} (v_k v_i + w_k w_i) (v_j v_h + w_j w_h) ds \\
 D_{kijh}^I &= \int_b A_{66} w_k w_{i,s} w_{j,s} w_h ds \\
 D_{kijh}^{II} &= \int_b A_{12} (v_k v_i + w_k w_i) w_{j,s} w_{h,s} ds \\
 B_{kijh} &= \int_b A_{22} w_{k,s} w_{i,s} w_{j,s} w_{h,s} ds.
 \end{aligned} \tag{9}$$

Note that  $A_{ij}$  and  $D_{ij}$  are the axial and bending stiffness matrices of each wall element, which can be evaluated by means of the following expressions<sup>32</sup>

$$A_{ij} = \int_t Q_{ij} dz = t Q_{ij} \quad D_{ij} = \int_t z^2 Q_{ij} dz = \frac{1}{12} t^3 Q_{ij}. \tag{10}$$

**2.2. Virtual work of the external loads**

Next, one must address the virtual work ( $\delta\Pi$ ) done by the external loads, which are assumed to belong to one of the following two types: (i) loads distributed over the member volume and (ii) “concentrated” loads applied on the member end sections (which are, in fact, distributed over the corresponding cross-section areas).

*2.2.1. Distributed loads*

Consider the applied load density per unit mid-surface area  $q(s, x) \equiv q$  as shown in Fig. 3(a), decomposed along the coordinate axes as  $q_x, q_s$  and  $q_z$  (see Fig. 3(b)). Note that, when body forces (e.g., gravity loads) are present, the value of  $q$  already incorporates the integration over the wall thickness. Then, the virtual work done by this load ( $\delta\Pi_q$ ) reads ( $\delta u, \delta v, \delta w$  are virtual displacements) as

$$\delta\Pi_q = - \int_L \int_b (q_x \delta u + q_s \delta v + q_z \delta w) ds dx \tag{11}$$

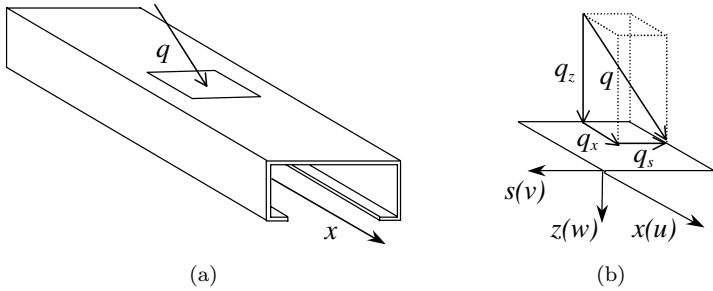


Fig. 3. (a) Applied load density  $q(x, s) \equiv q$  and (b) its components  $q_x, q_s$  and  $q_z$ .

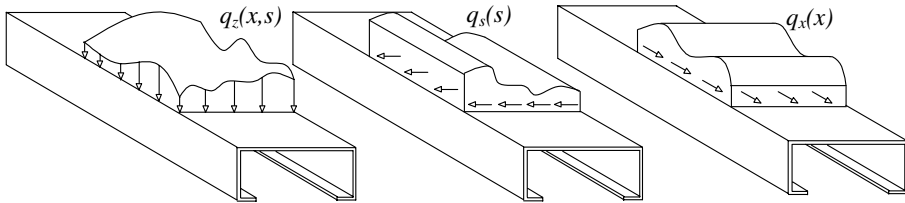


Fig. 4. Examples of load component distributions.

or, after introducing Eq. (1) (summation convention in  $i$ ),

$$\delta \Pi_q = - \int_L q_h dx \delta \phi_h - q_x u_h \delta \phi_h \Big|_0^L . \tag{12}$$

The load vector  $q_h$ , which is able to handle any load component distribution along the cross-section mid-line ( $s$ ) or the member axis ( $x$ ) (see Fig. 4), is given by

$$q_h = \int_b (q_s v_h + q_z w_h - q_{x,x} u_h) ds . \tag{13}$$

### 2.2.2. Concentrated end loads

Consider now the member end sections ( $x = 0; L$ ) subjected to a general applied stress distribution varying (i) linearly along the wall thickness (with  $z$ ) and (ii) arbitrarily along the cross-section mid-line (with  $s$ ). In the context of GBT, it is convenient to make a distinction between the applied stress components normal and tangential to the cross-section plane: “normal stresses”  $\sigma(s, z)$  and “shear stresses”  $\tau(s, z)$  (see Fig. 5).

Given the modal nature of GBT, it will be necessary to further decompose, either exactly or approximately, the applied stress distributions  $\sigma(s, z)$  and  $\tau(s, z)$  into a linear combination of a sequence of normal ( $\sigma_h(s, z)$ ) and shear ( $\tau_h(s, z)$ ) stress diagrams, each associated to a given deformation mode  $h$ . Since GBT deals with stress resultants, instead of stresses, the diagrams  $\sigma_h(s, z)$  and  $\tau_h(s, z)$  are naturally “replaced” by their counterparts  $W_h^\sigma$  and  $W_h^\tau$ . For instance, if  $h$  is the

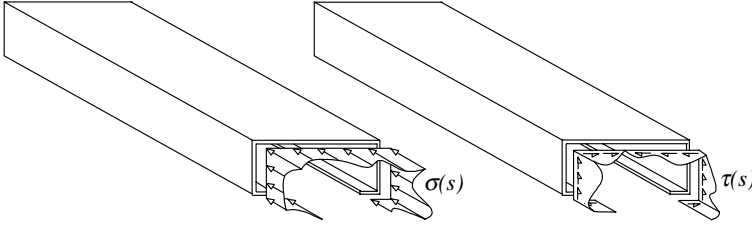


Fig. 5. Normal  $\sigma(s, z)$  and shear  $\tau(s, z)$  stress distributions applied at an end section.

major axis bending deformation mode, then  $W_h^\sigma$  is the applied major axis bending moment and  $W_h^\tau$  is the minor axis applied shear force. Then, the virtual work done by the stress resultants acting on the member end sections ( $x = 0; L$ ) reads as

$$\delta\Pi_W = -W_h^\sigma \delta\phi_{h,x}|_0^L - W_h^\tau \delta\phi_h|_0^L. \tag{14}$$

### 2.3. System of equilibrium equations

Applying the principle of virtual work and noting that  $\delta\phi_i$  are kinematically admissible and otherwise arbitrary functions, one obtains the system of member equilibrium equations, which can be written in a variational form, as

$$\delta U_1 + \delta U_2 + \delta U_3 - \delta \bar{U}_1 - \delta \bar{U}_2 - \delta \bar{U}_3 + \delta \Pi_q + \delta \Pi_W = 0. \tag{15}$$

The steps and procedures involved in the performance of a GBT post-buckling analysis are related to two main tasks: (i) *cross-section* and (ii) *member* analyses.<sup>28,33</sup> The first one concerns the identification of the deformation modes and the evaluation of the corresponding modal mechanical properties, i.e., the second, third and fourth order tensor quantities defined in Eq. (9). The second task aims at determining the evolution of functions  $\phi_k(x)$  with the load parameter  $\lambda$  and involves establishing and solving the system formed by Eq. (15). Obviously, it requires information on the cross-section modal mechanical properties, the member length, the end conditions and the applied load.

## 3. Cross-Section Analysis: Deformation Modes and Modal Mechanical Properties

The performance of a cross-section analysis requires a rather lengthy and relatively complex set of operations. Although these operations have been reported in the literature,<sup>11,28,31</sup> an overview presented herein puts them into perspective and, hopefully, it will help the reader in acquiring further insight on the unique features of GBT. Indeed, attention should be paid to the following points:

- (i) As mentioned earlier, the member cross-section (comprising  $n$  wall segments) must be discretized into  $n + 1$  natural nodes and  $m$  intermediate nodes.
- (ii) There are two families of deformation modes, namely, the *fundamental* modes (FM) and the *shear* modes (SM). The first designation accounts for the fact

that the FM are the modes originally considered by Schardt<sup>11</sup> (the SM have only very recently been addressed).<sup>31,34</sup>

(iii) The FM constitute the core of GBT and are based on Vlassov's hypothesis of neglecting the in-plane (membrane) shear deformations ( $\gamma_{xs}^M = 0$ ) in the member walls. Therefore, all FM are *shear nondeformable*. They can still be divided into two sub-groups, depending on whether they stem from warping displacements  $u$  (FM<sub>*u*</sub>) or flexural displacements  $w$  (FM<sub>*w*</sub>):

- The FM<sub>*u*</sub> are the essence of GBT and always correspond to non-null displacements  $u(s)$ ,  $v(s)$  and  $w(s)$ , obtained by imposing unit warping displacements at each natural node and taking into account geometrical relations based on Vlassov's hypothesis. Moreover, these modes include all the deformation modes considered by the classical beam theories, such as Euler–Bernoulli or Vlassov theories.
- The FM<sub>*w*</sub>, somewhat departing from the “pure essence” of GBT, are associated to transverse bending of the member walls (no warping). The  $w(s)$  are the only non-null displacements, obtained by imposing unit flexural displacements at each intermediate node. Since  $u(s) = v(s) = 0$ , all FM<sub>*w*</sub> trivially satisfy Vlassov's hypothesis.

(iv) Up until very recently, the incorporation of SM in GBT had never been raised, probably because the influence of shear deformation on either the first order or linear stability behavior of isotropic thin-walled members is negligible. Since SM violates Vlassov's assumption, their determination must be based on other hypotheses. Depending on the nature of these hypotheses, SM may also be divided into the following two sub-groups:

- SM<sub>*u*</sub>, based on the assumption of  $v(s) = 0$  and, therefore, involving only warping and flexural displacements  $u(s)$  and  $w(s)$ , obtained by imposing unit warping displacements and null membrane transverse displacements at each natural and intermediate node. Since this implies the absence of flexural displacements  $w(s)$ , the cross-section experiences no in-plane deformation (it does not even move).
- SM<sub>*v*</sub>, based on the assumption of  $u(s) = 0$  and, thus, involving only transverse displacements  $v(s)$  and  $w(s)$ , obtained by imposing unit membrane transverse displacements and null warping displacements at each node: (a) two such displacements at each “internal” natural node (along the transverse directions of the converging wall elements) and (b) one at the two “end” natural nodes and each intermediate node. As the imposition of  $v_k = 1$  at a wall element converging at a given natural node always leads to flexural displacements  $w(s)$  at the adjacent wall element, these modes involve in-plane cross-section deformation. The inclusion of the SM<sub>*v*</sub> makes it possible to account for the cross-section deformation stemming from the plate elements transverse extension.

(v) In order to satisfy all different mode assumptions, the cross-section deformed configurations due to the application of the “unit functions” are “constrained” in such a way that compatibility between displacements  $u_k(s)$ ,  $v_k(s)$  and  $w_k(s)$  is ensured. Therefore, the corresponding displacement field is characterized by:

- $FM_u$ : linear  $u_k(s)$ , constant  $v_k(s)$  and cubic  $w_k(s)$ .
- $FM_w$ :  $u_k(s) = v_k(s) = 0$  and cubic  $w_k(s)$ .
- $SM_u$ : linear  $u_k(s)$  and  $v_k(s) = w_k(s) = 0$ .
- $SM_v$ :  $u_k(s) = 0$ , linear  $v_k(s)$  and constant  $w_k(s)$ .

(vi) After determining the displacement field, calculating the tensor quantities defined in Eq. (9) becomes a straightforward (but time-consuming) task, which can be performed using a symbolic manipulation (e.g., MAPLE).<sup>35</sup> Note, however, that, with just a few exceptions, all the tensor components are non-null, thus implying that the associated GBT system of nonlinear equations [Eqs. (15)] is *highly coupled*. In order to take full advantage of the GBT potential and shed light on the physical meaning of the components of matrices (second order tensors)  $[C_{kh}]$ ,  $[B_{kh}]$  and  $[D_{kh}]$ , the previous “(generalized) coordinates” must be changed so that two of the above three matrices become *simultaneously diagonal*. In order to define such coordinate change, one must solve four eigenvalue problems (one per deformation mode sub-group):

- $FM_u$ :  $([B_{kh}] - \lambda[C_{kh}])u_k = \{0\}$ .
- $FM_w$ :  $([B_{kh}] - \lambda[C_{kh}])w_k = \{0\}$ .
- $SM_u$ :  $([D_{kh}] - \lambda[C_{kh}])u_k = \{0\}$ .
- $SM_v$ :  $([B_{kh}] - \lambda[D_{kh}])v_k = \{0\}$ .

(vii) The solution of the four eigenvalue problems leads to the identification of sets of eigenvectors  $\{a_k\}$  corresponding to orthogonal cross-section *deformation modes*. For instance, the modes yielded by solving the first ( $FM_u$ ) eigenvalue problem are: extension, major axis bending, minor axis bending, torsion and several distortion modes. After applying the transformation matrix (assemblage of the eigenvectors  $\{a_k\}$ ) to  $[C_{kh}]$ ,  $[B_{kh}]$  and  $[D_{kh}]$ , one is led to “transformed matrices” whose components are *cross-section mechanical properties*. Their physical meanings are obvious for the four  $FM_u$  global modes (axial, bending, torsion and warping stiffness values) and unfamiliar, for the distortional  $FM_u$ ,  $FM_w$  and  $SM$ . A detailed description of the techniques used to obtain these results can be found in work by the authors.<sup>11,28,31</sup>

Table 1 provides an overall view of the hypotheses, steps and procedures involved in performing a GBT cross-section analysis. Finally, in order to enable the visualization of the different deformation modes, Figs. 6–9 show, for the case of a lipped channel cross-section, the most relevant features of the four sets of GBT modes: (i) the  $FM_u$  and  $FM_w$  in-plane configurations ( $v_k$  and  $w_k$ ), (ii) the  $SM_u$  warping displacements ( $u_k$ ) and (iii) the  $SM_v$  transverse ( $v_k$ ) and flexural ( $w_k$ ) displacements.

Table 1. Steps and procedures involved in aGBT cross-section analysis.

	FM <sub>u</sub>	FM <sub>w</sub>	SM <sub>u</sub>	SM <sub>v</sub>
I	Cross-section discretization	$n + 1$ natural nodes (NN) and $m$ intermediate nodes (IN)		
II	Imposition of unit nodal displacements	$u_k = 1$ (NN)	$u_k = 1$ (NN + IN)	$v_k = 1$ (NN + IN)
III	Hypothesis	Vlasov ( $\gamma_{x's}^M = 0$ ) $u_{k,s} + v_k = 0$	$u_k = v_k = 0$	$u_k = 0$
IV	Evaluation of the displacement field	$u(s) \in P_0$ $v(s) \in P_1$ $w(s) \in P_3$	$w(s) \in P_3$ $u(s) \in P_1$	$v(s) \in P_1$ $w(s) \in P_0$
V	Matrix calculation	Full matrices with no physically meaningful components		
VI	Determination of the deformation modes	$([B_{kh}] - \lambda[C_{kh}]) \times u_k = 0$	Eigenvalue problem $([D_{kh}] - \lambda[C_{kh}]) \times u_k = 0$	$([B_{kh}] - \lambda[D_{kh}]) \times v_k = 0$
VII	Evaluation of cross-section modal properties	Matrices calculated using modal displacement fields and with physically meaningful components		

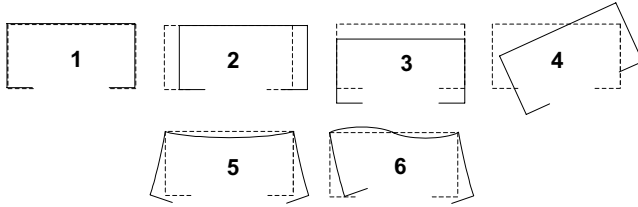


Fig. 6. In-plane ( $v_k, w_k$ ) configurations of the  $FM_u$  (global and distortional) modes.

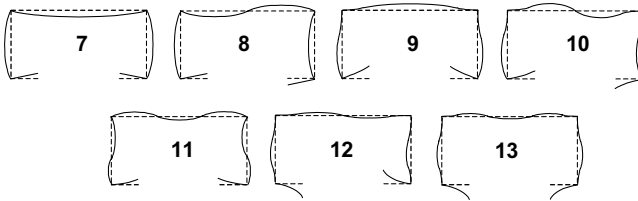


Fig. 7. In-plane ( $v_k, w_k$ ) configurations of the  $FM_w$  (local-plate) modes.

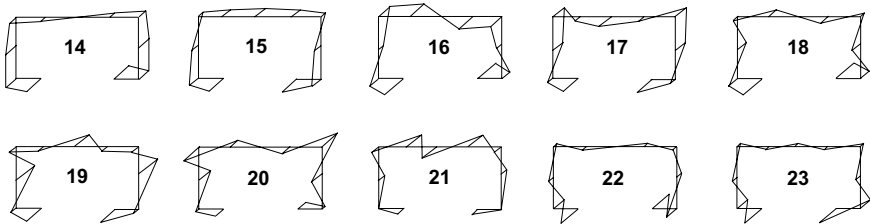


Fig. 8. Warping displacements ( $u_k$ ) associated to the  $SM_u$  modes.

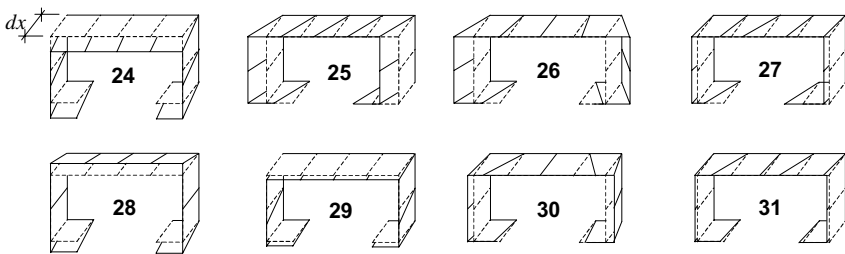


Fig. 9. Transverse ( $v_k$ ) and flexural ( $w_k$ ) displacements associated to the  $SM_v$  modes.

### 4. Member Analysis: FEM Solution of the GBT Equations

#### 4.1. Nonlinear beam FE formulation

In order to solve the system of GBT nonlinear equations [Eq. (15)], a beam FE is formulated, using Hermitean polynomials to approximate the deformation mode amplitude functions  $\phi_k(x)$ , i.e. by adopting the shape function vector

$$\mathbf{N} = [L_e(\xi^3 - 2\xi^2 + \xi) \quad 2\xi^3 - 3\xi^2 + 1 \quad L_e(\xi^3 - \xi^2) \quad -2\xi^3 + 3\xi^2] , \quad (16)$$

where  $L_e$  is the FE length and  $\xi = x/L_e$ . The vector of generalized nodal displacements is

$$\mathbf{d}_k = [d_{k1} \quad d_{k2} \quad d_{k3} \quad d_{k4}]^\top , \quad (17)$$

with  $d_{k1} = \phi_{k,x}(0)$ ,  $d_{k2} = \phi_k(0)$ ,  $d_{k3} = \phi_{k,x}(L_e)$ ,  $d_{k4} = \phi_k(L_e)$ . Incorporating

$$\phi_k(x) = \mathbf{N} \cdot \mathbf{d}_k , \quad (18)$$

into Eq. (15) and carrying out the integrations, one is led to the FE matrix equation

$$\mathbf{f}^{(e)} = \mathbf{f}_e^{(e)} \Leftrightarrow \mathbf{f}_1^{(e)} + \mathbf{f}_2^{(e)} + \mathbf{f}_3^{(e)} - \bar{\mathbf{f}}_1^{(e)} - \bar{\mathbf{f}}_2^{(e)} - \bar{\mathbf{f}}_3^{(e)} = \mathbf{f}_e^{(e)} , \quad (19)$$

where  $\mathbf{f}_e^{(e)}$  is the external applied force vector,  $\mathbf{f}_p^{(e)}$  are internal force vectors whose components are linear ( $p = 1$ ), quadratic ( $p = 2$ ) or cubic ( $p = 3$ ) functions of the  $\mathbf{d}^{(e)}$  components, and  $\bar{\mathbf{f}}_p^{(e)}$  are (additional) internal force vectors related to the initial geometric imperfections whose components are linear ( $p = 1$ ), linear and quadratic ( $p = 2$ ) and quadratic ( $p = 3$ ) functions of the imperfection  $\bar{\mathbf{d}}^{(e)}$ . Note also that (i)  $\bar{\mathbf{f}}_1^{(e)}$  components are independent of  $\mathbf{d}^{(e)}$ , (ii) some  $\bar{\mathbf{f}}_3^{(e)}$  components vary linearly with  $\bar{\mathbf{d}}^{(e)}$  and (iii)  $\bar{\mathbf{f}}_2^{(e)}$  components include terms independent and linear in  $\bar{\mathbf{d}}^{(e)}$ . Vectors  $\mathbf{f}_p^{(e)}$  are expressed in the form

$$\mathbf{f}_p^{(e)} = \mathbf{K}_{p-1}^{(e)} \mathbf{d}^{(e)} \quad \left( \sum_{p=1}^3 \mathbf{K}_{p-1}^{(e)} \right) \mathbf{d}^{(e)} = \mathbf{f}_e^{(e)} , \quad (20)$$

where displacement vector  $\mathbf{d}^{(e)}$ , external force vector  $\mathbf{f}_e^{(e)}$  and stiffness matrix  $\mathbf{K}_{p-1}^{(e)}$  are given by ( $N$  is the number of cross-section deformation modes)

$$\mathbf{d}^{(e)} = \begin{Bmatrix} \mathbf{d}_1 \\ \dots \\ \mathbf{d}_k \\ \dots \\ \mathbf{d}_N \end{Bmatrix} \quad \mathbf{f}_e^{(e)} = \begin{Bmatrix} \mathbf{f}_1 \\ \dots \\ \mathbf{f}_h \\ \dots \\ \mathbf{f}_N \end{Bmatrix} \quad \mathbf{K}_{p-1}^{(e)} = \begin{bmatrix} \mathbf{k}_{11}^{p-1} & \dots & \mathbf{k}_{1h}^{p-1} & \dots & \mathbf{k}_{1N}^{p-1} \\ \dots & \dots & \dots & \dots & \dots \\ \mathbf{k}_{k1}^{p-1} & \dots & \mathbf{k}_{kh}^{p-1} & \dots & \mathbf{k}_{kN}^{p-1} \\ \dots & \dots & \dots & \dots & \dots \\ \mathbf{k}_{N1}^{p-1} & \dots & \mathbf{k}_{Nh}^{p-1} & \dots & \mathbf{k}_{NN}^{p-1} \end{bmatrix} , \quad (21)$$

where the sub-matrix  $\mathbf{k}_{kh}^{p-1}$  components concern either single deformation mode  $k(k = h)$  or coupling between two, three or four modes ( $k \neq h$ ), and the sub-vector  $\mathbf{f}_h$ , related to the work done by the external forces when the cross-section deforms in mode  $h$ , reads

$$\mathbf{f}_h = q_h \mathbf{f}_1 + W_h^\sigma \mathbf{f}_2 + W_h^\tau \mathbf{f}_3 + u_h \mathbf{f}_4 . \quad (22)$$

$\mathbf{K}_0^{(e)}$  is the linear stiffness matrix (symmetric and independent of  $\mathbf{d}^{(e)}$ ), with components

$$\mathbf{k}_{kh}^0 = C_{kh} \mathbf{k}_1 + D_{kh}^I \mathbf{k}_2 + D_{kh}^{II} \mathbf{k}_3 + D_{hk}^{II} \mathbf{k}_3^T + B_{kh} \mathbf{k}_4, \quad (23)$$

and  $\mathbf{K}_1^{(e)}$  and  $\mathbf{K}_2^{(e)}$  are nonlinear stiffness matrices (dependent on  $\mathbf{d}^{(e)}$  and often non-symmetric), with sub-matrices  $\mathbf{k}_{kh}^1$  and  $\mathbf{k}_{kh}^2$  having components which vary linearly and quadratically with  $\mathbf{d}^{(e)}$  and are given by

$$\begin{aligned} \mathbf{k}_{kh}^1 = & C_{kjh} \mathbf{k}_5 + \frac{1}{2} C_{hjk} \mathbf{k}_6 + \left( B_{kjh} + \frac{1}{2} B_{hjk} \right) \mathbf{k}_7 \\ & + D_{kjh}^I \mathbf{k}_8 + (D_{hjk}^I + D_{khj}^I) \mathbf{k}_9 + \frac{1}{2} D_{hjk}^{II} \mathbf{k}_{10} + D_{kjh}^{II} \mathbf{k}_{11} \\ & + D_{kjh}^{III} \mathbf{k}_{12} + \frac{1}{2} D_{hjk}^{III} \mathbf{k}_{13}, \end{aligned} \quad (24)$$

$$\begin{aligned} \mathbf{k}_{kh}^2 = & \frac{1}{2} C_{kijh} \mathbf{k}_{14} + \frac{1}{2} B_{kijh} \mathbf{k}_{15} + D_{kijh}^I \mathbf{k}_{16} + D_{kihj}^I \mathbf{k}_{17} \\ & + \frac{1}{2} D_{kijh}^{II} \mathbf{k}_{18} + \frac{1}{2} D_{jhki}^{II} \mathbf{k}_{19}. \end{aligned} \quad (25)$$

Obviously, the expressions providing the components of matrices  $\mathbf{k}_5 - \mathbf{k}_{19}$  are much more complex than the ones related to matrices  $\mathbf{k}_1 - \mathbf{k}_4$ . For illustrative purposes, the components of matrices  $\mathbf{k}_1 - \mathbf{k}_5$  and vectors  $\mathbf{f}_1 - \mathbf{f}_4$  are supplied in the Appendix.

Then, one is led to the matrix equation

$$(\mathbf{K}_0^{(e)} + \mathbf{K}_1^{(e)} + \mathbf{K}_2^{(e)}) \mathbf{d}^{(e)} - (\mathbf{K}_0^{(e)} + \bar{\mathbf{K}}_1^{(e)} + \bar{\mathbf{K}}_2^{(e)}) \bar{\mathbf{d}}^{(e)} = \mathbf{f}_e^{(e)}, \quad (26)$$

where matrices  $\mathbf{K}_p^{(e)}$  can be viewed as *secant* stiffness matrices. The solution of Eq. (26) requires the definition of the symmetric tangent stiffness matrix

$$\mathbf{T}_{ij}^{(e)} = \mathbf{K}_{0ij}^{(e)} + \frac{\partial}{\partial \mathbf{d}_j^{(e)}} (\mathbf{f}_2^{(e)} + \mathbf{f}_3^{(e)} - \bar{\mathbf{f}}_2^{(e)} - \bar{\mathbf{f}}_3^{(e)})_i, \quad (27)$$

which may be obtained either directly from the second variation of the discretized member strain energy  $\delta^2 U$  [Eqs. (7) and (8)], or by differentiating the internal force vector components ( $\mathbf{f}_p^{(e)}$ ) [see Eq. (19)].

#### 4.2. FE implementation and incremental-iterative solution technique

The FE implementation of the nonlinear GBT involves the following tasks:

- (i) Selecting the GBT deformation modes to be considered, which define the sub-system of nonlinear equilibrium equations to be solved.
- (ii) Longitudinal discretization (number of FEs —  $n_e$ ).
- (iii) Identification of the (nodal) degrees of freedom, which are grouped in a global displacement vector  $\mathbf{d}$  and account for the end support conditions.

- (iv) Assembling the FE internal and external force vectors [see Eqs. (19) or (26)] into global ones ( $\mathbf{f}$  and  $\mathbf{f}_e$ ).
- (v) Assembling all FE tangent stiffness matrices into a global tangent matrix ( $\mathbf{T}$ ).
- (vi) Solving the nonlinear equations, using a predictor-corrector technique based on the application of Newton–Raphson’s method and arc-length control.
- (vii) Post-processing and interpreting the results (stresses and displacements).

The diagrams presented in Figs. 10 and 11 provide overall views of the main steps and procedures involved in GBT post-buckling analysis of a thin-walled cold-formed steel (isotropic) member and the incremental-iterative solution of the nonlinear equations.

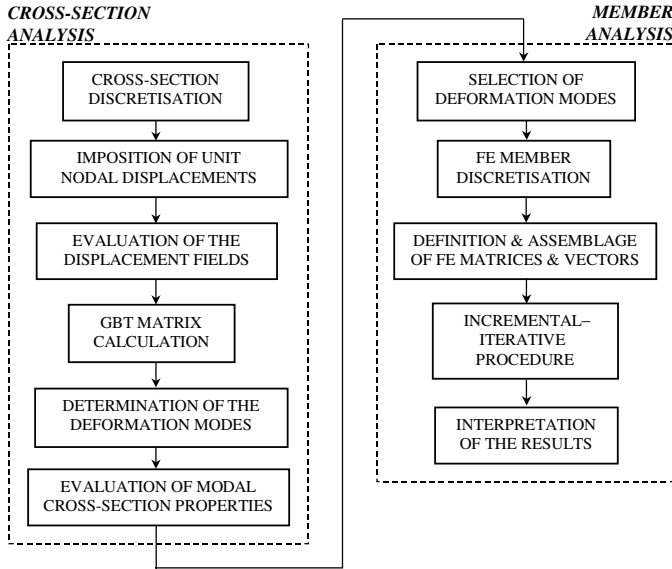


Fig. 10. Diagram of the GBT post-buckling analysis of a member.

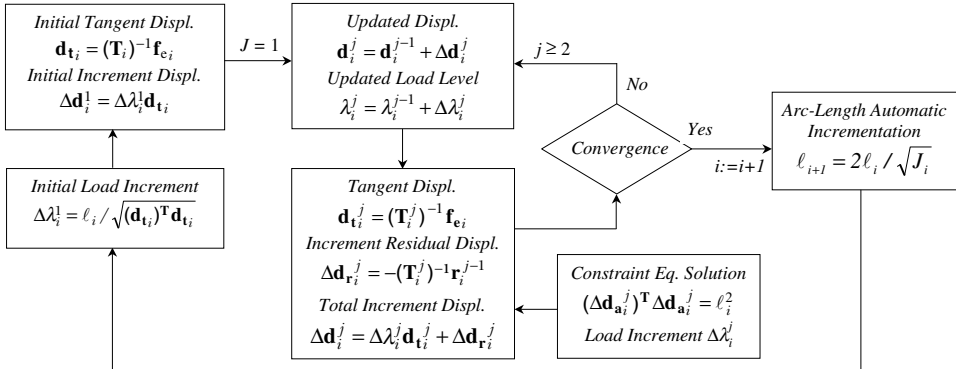


Fig. 11. Diagram of incremental-iterative solution of nonlinear equations.

Since information on the Newton–Raphson’s method and arc-length control techniques is available in the literature,<sup>2,36</sup> the latter diagram is sketched rather concisely. Note that the subscript  $i$  denotes the  $i$ th load step, the superscript  $j$  denotes the  $j$ th iterative cycle within the  $i$ th load step and convergence at the end of the  $(i - 1)$ th load step is assumed, i.e., configuration  $(\lambda_{i-1}, \mathbf{d}_{i-1})$  satisfies equilibrium ( $\lambda$  is the load parameter). Finally, a few remarks about the arc-length control strategy adopted:

- (i) The initial increment of the first load step ( $\Delta\lambda_1^j$ ) is a fixed percentage of the known (*calculated a priori*) member critical load  $\lambda_{cr}$ .
- (ii) The calculation of  $\Delta\lambda_i^j$  (load parameter increment), needed to evaluate  $\Delta\mathbf{d}_i^j$ , requires solving a constraint equation proposed by Crisfield.<sup>2,36</sup>
- (iii) Automatic increment of the arc-length value ( $\ell_i$ ) is adopted: the current  $\ell_i$  is deemed constant within a load step and the next value  $\ell_{i+1}$  (valid for load step  $i + 1$ ) is automatically changed, on the basis of  $\ell_i$ .

It is important, at this stage, to emphasize that accurate post-buckling results can often be obtained by solving just a selected (small) subsystem of Eq. (26) because, in many cases, the post-buckling evolution of the member deformed configuration involves only a few deformation modes, i.e., GBT *cross-section degrees of freedom*. Thus, if one just solves the subsystem of Eq. (26) formed by the equations related to those modes, it is possible to reduce the computational effort (CPU time) significantly, while still retaining a high accuracy. It all amounts to approximating the member deformed configuration exclusively by the selected modes, an approach that cannot be followed when employing other discretization methods, such as the finite strip method. Indeed, it is not possible to describe the cross-section deformed configuration by means of a few *nodal displacements and rotations*.

## 5. Illustrative Examples

In order to validate and illustrate the application and capabilities of the proposed nonlinear GBT and corresponding FEM implementation, several numerical results are presented. They concern the post-buckling behavior of uniformly compressed plates and lipped channel and Z-section columns. In the latter case, the stub-columns analyzed buckle in both the local-plate and distortional modes. All post-buckling analyses assume a material (steel) behavior characterized by  $E = 200$  MPa and  $\nu = 0.3$  and include initial geometrical imperfections with the critical buckling mode shape, obtained from preliminary linear stability analyses, and small amplitudes.

### 5.1. Uniformly compressed plates

The uniformly compressed simply supported square plate ( $b = L$ ) shown in Fig. 12(a), which contains a critical-mode initial imperfection with amplitude

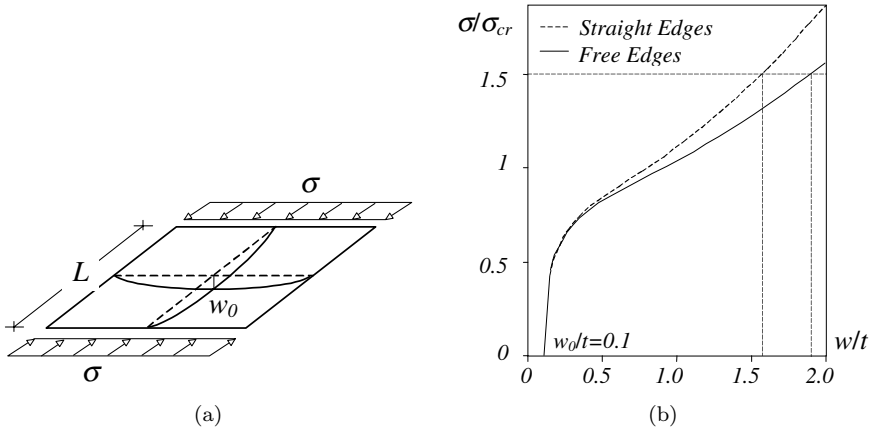


Fig. 12. Uniformly compressed simply supported square plate: (a) initial configuration and (b) post-buckling equilibrium paths.

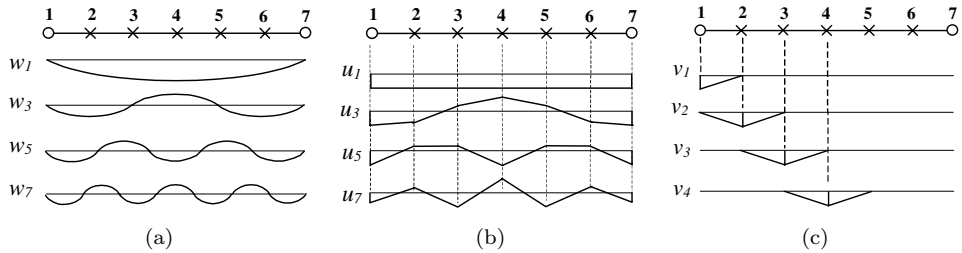


Fig. 13. Plate deformation modes: (a)  $FM_w(w_i)$ , (b)  $SM_u(u_i)$  and (c)  $SM_v(v_i)$ .

$w_0 = 0.1t$  ( $t$  is the plate thickness) was analyzed in two situations: unloaded edges (i) forced to remain straight and (ii) free to deform transversally. The GBT deformation modes associated with a “cross-section” discretization in seven nodes are displayed in Figs. 13(a)–(c). Note also that (i) only  $FM_w$  with odd half-wave numbers participate in the plate buckling mode (obviously, the first one is predominant), (ii) one must include  $SM_v$  to obtain accurate post-buckling results for the free-edge plate and (iii)  $SM_u$  play a minor role.

In order to assess the convergence of the FEM implementation, one first compares the results obtained with different plate discretizations, i.e., numbers of nodes ( $n_n$ ) and FE ( $n_e$ ). Table 2 gives the  $w/t$  values ( $w$  is the displacement at the plate

Table 2. Variation of the  $w/t$  value at  $\sigma/\sigma_{cr} = 1.5$  with  $n_n$  and  $n_e$ .

	Free-edge Plate				Straight-edge Plate		
	$n_e = 6$	$n_e = 8$	$n_e = 10$		$n_e = 6$	$n_e = 8$	$n_e = 10$
$n_n = 7$	1.57	1.62	1.62	$n_n = 7$	1.48	1.50	1.50
$n_n = 9$	1.72	1.88	1.88	$n_n = 9$	1.56	1.59	1.59
$n_n = 11$	1.86	1.88	1.88	$n_n = 11$	1.58	1.59	1.59

center) for an applied stress  $\sigma/\sigma_{cr} = 1.5$  [see Fig. 12(b)] and different combinations of  $n_n$  and  $n_e$ . The results show that convergence is achieved, both for the free-edge and straight-edge plates, if 9 nodes and 8 elements are considered. The corresponding  $w/t$  values ( $w/t = 1.88$  and  $w/t = 1.59$ ) practically coincide with the ones reported by Prola<sup>14</sup> and obtained using the spline finite strip method ( $w/t = 1.92$  and  $w/t = 1.61$ ).

The post-buckling equilibrium paths displayed in Fig. 12(b) concern the free-edge and straight-edge plates and were obtained with the “optimal discretization” ( $n_n = 9$  and  $n_e = 8$ ). The comparison between the two curves confirms the well-known difference exhibited by the post-buckling behaviors of the two plates and the GBT analysis shows clearly that it stems from restricting the participation of the  $SM_v$  in the straight-edge case (thus inducing tensile transverse membrane stresses, responsible for the additional stiffness). Moreover, the two equilibrium paths also follow very closely the spline finite strip curves determined by Prola.<sup>14</sup>

Finally, note that “approximate post-buckling analyses”, including only the  $SM_v$  and the single half-wave  $FM_w$ , yield  $w/t = 1.48$  (straight-edge plate) and  $w/t = 1.75$  (free-edge plate). This means that one captures about 90% of the exact  $w/t$  value (the 3 and 5 half-wave  $FM_w$  account for the remaining 10%) with considerably less computation.

### 5.2. Lipped channel columns

The lipped channel columns analyzed have pinned and free-to-warp end sections and cross-section dimensions  $b_{web} = b_{flange} = 150$  mm,  $b_{lip} = 7.5$  mm and  $t = 1.5$  mm. The discretizations involve 6 natural nodes, 17 intermediate nodes (5 in the web and flanges and 1 in each lip) and 8 finite elements. Since it is intended to determine local-plate (LP) and distortional (D) post-buckling equilibrium paths, a preliminary stability analysis was needed to evaluate the stub-column lengths associated to critical single half-wave LPM and DM ( $L_{LP}$ ,  $L_D$ ) and corresponding bifurcation stresses ( $\sigma_{cr}^{LP}$ ,  $\sigma_{cr}^D$ ): (i)  $L_{LP} = 120$  mm and  $\sigma_{cr}^{LP} = 70.6$  MPa and (ii)  $L_D = 637$  mm and  $\sigma_{cr}^D = 31.8$  MPa.

The post-buckling analyses include all deformation modes ( $FM_u$ ,  $FM_w$ ,  $SM_u$  and  $SM_v$ ) and, since the configurations of most of them have been shown in Figs. 6–9, only the ones relevant for the column post-buckling behavior are identified next: (i) extension (**1**), minor axis bending (**3**) and distortional (**5**)  $FM_u$  modes (Fig. 6); (ii) primary (**7**) and secondary (**9**, **11**, **13**) local-plate  $FM_w$  modes (Fig. 7); (iii)  $SM_u$  shear modes (**15–23**) (Fig. 8); (iv)  $SM_v$  transverse extension modes (**24–31**) (Fig. 9).

All stub-columns have critical-mode initial imperfections with amplitudes  $w_0 = 0.1t$  (LPM —  $w_0$  is the initial mid-web flexural displacement) or  $v_0 = \pm 0.01t$  (DM —  $v_0$  is the initial lip transverse membrane displacement). Since the degree of nonlinearity of the LPM and DM post-buckling equilibrium paths is distinct,<sup>14</sup> different first load increments  $\Delta\lambda_1^1$  were chosen: 15% (LPM) and 7.5% (DM) of the critical load.

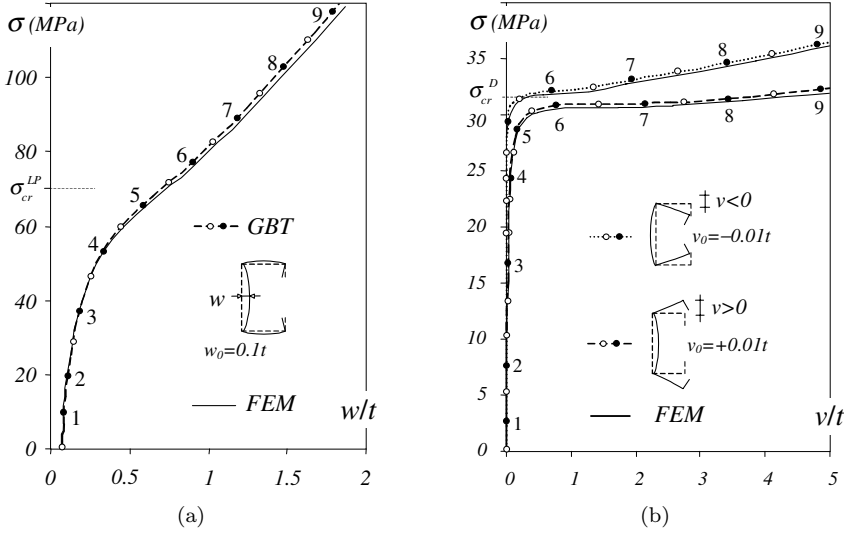


Fig. 14. Post-buckling equilibrium paths of lipped channel columns: (a) LP (b) D.

Figure 14(a) compares LP post-buckling paths obtained using (i) the GBT approach and (ii) the FEM code ABAQUS<sup>37</sup> (fine mesh of shear deformable S4 shell FE). Although the results are reported in terms of the mid-web displacement  $w$ , the column instability is triggered by the *flanges* (recall that one has  $b_{\text{flange}} = b_{\text{web}}$ ). Figure 14(b), on the other hand, shows four D post-buckling paths, yielded by GBT and FEM (ABAQUS) analyses of two identical columns with different initial imperfections: (i)  $v_0 = +0.01t$  (flange-lip assemblies “open”) and (ii)  $v_0 = -0.01t$  (flange-lip assemblies “close”). One realizes immediately that, as recently reported by Prola,<sup>14</sup> the D post-critical strength is much smaller than its LP counterpart (regardless of the  $v_0$  sign). In addition, the observation of the above curves leads to the following remarks:

- (i) The match between GBT and FEM (ABAQUS) curves is virtually perfect. For instance, (i<sub>1</sub>) for  $\sigma = \sigma_{cr}^{LP}$ , one has  $(w/t)_{\text{GBT}} = 0.63$  and  $(w/t)_{\text{FEM}} = 0.64$ , and (i<sub>2</sub>) for  $v_0/t = -0.01$  and  $\sigma = \sigma_{cr}^D$ , one has  $(v/t)_{\text{GBT}} = 0.320$  and  $(v/t)_{\text{FEM}} = 0.326$ .
- (ii) The dependence of the column D post-buckling behavior on the  $v_0$  sign is not negligible, as recently unveiled by Prola and Camotim.<sup>38</sup> They attributed this post-buckling *asymmetry* (higher post-critical strength for  $v_0/t < 0$ ) to marked differences in the warping behavior of the flanges and (mostly) the lips.
- (iii) The curves associated to  $v_0/t = 0.01$  (dashed) and  $v_0/t = -0.01$  (dotted) begin to “split” well below the critical stress: for  $\sigma = \sigma_{cr}^D$ , one has already  $v/t = 3.84$  ( $v_0/t = 0.01$ ) and  $v/t = 0.32$  ( $v_0/t = -0.01$ ).

Next, one illustrates how the unique features of the nonlinear GBT can be used to either (i) improve the understanding about the column post-buckling behavior or

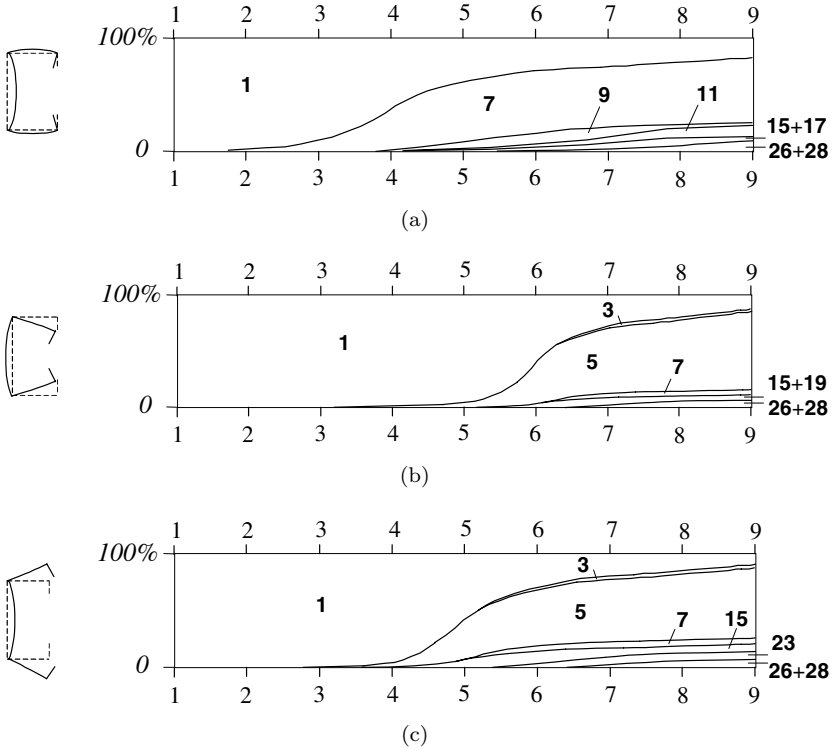


Fig. 15. Modal participation in the post-buckling path: (a) LP (b) D ( $v_0 < 0$ ) (c) D ( $v_0 > 0$ ).

(ii) develop computationally more efficient analyses. Figures. 15(a)–(c) show “GBT modal analyses” of the equilibrium paths shown in Figs. 14(a) and (b). These figures display the evolution of the deformation mode “degree of participation”<sup>a</sup> along the column post-buckling paths, thus shedding new light on several aspects concerning the deformed configuration. In particular, they provide an in-depth explanation for the D post-buckling asymmetry mentioned earlier.

The numbers 1–9 located along the top and bottom horizontal axes in Figs. 15(a)–(c) correspond to the equilibrium points identified by black dots in Figs. 14(a) and (b). Thus, line segments uniting identical numbers provide an assessment of the degree of participation (in percentage) of each GBT deformation mode on the deformed configuration. The main conclusions drawn from Figs. 15(a)–(c) are:

- (i) The extension mode (1) fully governs in the early pre-buckling stages of the three stub-columns. Its participation continuously decreases.

<sup>a</sup>The *exact* degree of participation of each mode  $k$  in the cross-section deformed configuration must be evaluated on the basis of  $\phi_k$  and, obviously, varies along the column length. The results reported here concern *average* degrees of participation, i.e., are based on the values of the quantities  $\int_0^L |\phi_k(x)| dx$ .

(ii) Concerning the LP behavior (Fig. 14(a)), one notices that:

- Mode **7** dominates. It appears at low applied stress values (near point 2) and progresses steadily, reaching a participation as high as 86%.
- Modes **9** and **11** become meaningful for  $\sigma_{LP} > 0.70\sigma_{cr}^{LP}$  and  $\sigma > 1.30\sigma_{cr}^{LP}$ .
- Shear modes **15** and **17** appear for  $\sigma > \sigma_{cr}^{LP}$  and their joint participation never exceeds 4%.
- Modes **26** and **28** only appear for  $\sigma > 1.30\sigma_{cr}^{LP}$ , but their joint participation quickly grows up to 5%.

(iii) Concerning the D behavior (Fig. 14(b)), it is to be noted that

- Mode **5** dominates, but its participation is quite different for positive and negative  $v_0/t$ . For  $v_0/t = 0.01$ , it appears at  $\sigma \approx 0.73\sigma_{cr}^D$  (near point 4) and progressively grows up to about 85%. For  $v_0/t = -0.01$ , it appears only at  $\sigma \approx 0.94\sigma_{cr}^D$  (near point 5), but grows faster to about 90%.
- The shear mode participation also differs for  $v_0/t = 0.01$  and  $-0.01$ . In the former case, modes **15** and **23** emerge (with mode 5) at  $\sigma \approx 0.73\sigma_{cr}^D$  and their participation is relevant (reaches 12%). In the latter case, these modes appear only for  $\sigma > \sigma_{cr}^D$  and never contribute more than 5%.
- The previous two items fully explain the D distortional post-buckling asymmetry exhibited by the curves presented in Fig. 14(b). It would be impossible to extract such an explanation from the results yielded by “conventional” finite strip or finite element analyses.
- Deformation modes **3** ( $FM_u$ ), **7** ( $FM_w$ ) and **26** + **28** ( $SM_v$ ) play similar roles for  $v_0/t = 0.01$  and  $-0.01$ .

The previous “GBT modal analyses” make it possible to assess the relevance (accuracy and computational efficiency) of including the different deformation modes in the LP and D post-buckling analyses. Concerning the accuracy, one compares the results yielded by various “GBT approximate analyses”, involving only selected subsets of the deformation modes identified in Figs. 15(a)–(c). These results are presented in Figs. 16 and 17 (for clarity, the lower portions of the curves are omitted and a larger vertical scale is used) and, for comparison purposes, the “exact” curves (all deformation modes) are shown again. The curves displayed in Fig. 16 (LP behavior) show that:

- (i) If only modes **1** and **7** are included (dotted curve), the  $w/t$  values are very accurate only up to  $\sigma \approx 0.80\sigma_{cr}^{LP}$  and progressively loose accuracy. However, the error never exceeds 15%: e.g., for  $\sigma = \sigma_{cr}^{LP}$  and  $\sigma = 1.50\sigma_{cr}^{LP}$ , one has  $(w/t)_{ap} = 0.54$  and  $(w/t)_{ap} = 1.32$ , instead of  $(w/t)_{ex} = 0.63$  and  $(w/t)_{ex} = 1.51$ .
- (ii) If only modes **1**, **7**, **9** and **11** are included (dashed curve), the  $w/t$  values are exact up to  $\sigma = \sigma_{cr}^{LP}$  and always remain fairly accurate. The error never exceeds 5%: e.g., for  $\sigma = 1.50\sigma_{cr}^{LP}$ , one has  $(w/t)_{ap} = 1.44$ , instead of  $(w/t)_{ex} = 1.51$ .

As for the curves displayed in Figs. 17(a) and (b), (D post-buckling behavior for  $v_0 = 0.01t$  and  $v_0 = -0.01t$ ), it is to be remarked that

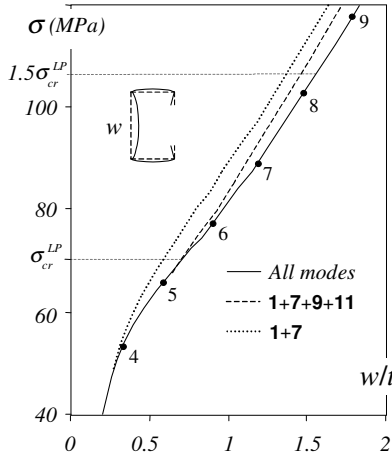


Fig. 16. Exact and approximate local-plate post-buckling paths.

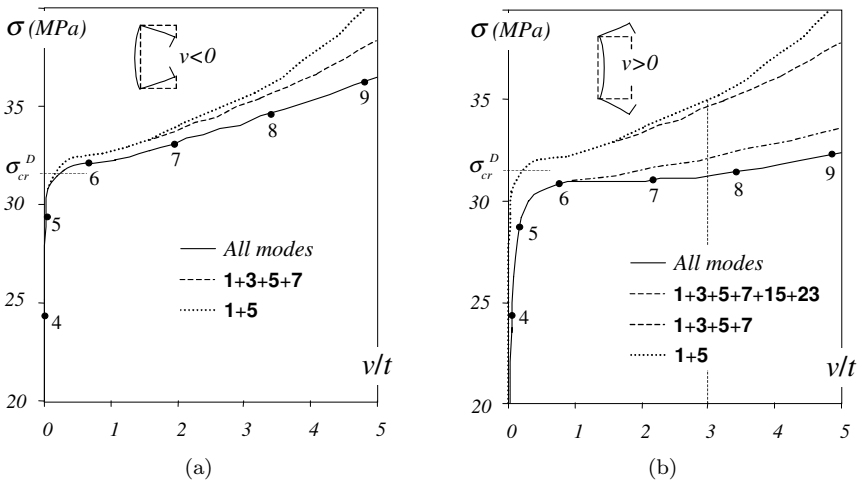


Fig. 17. Exact and approximate distortional post-buckling paths: (a)  $v_0 < 0$  (b)  $v_0 > 0$ .

- (i) If only modes **1** and **5** or **1, 3, 5** and **7** are included, the post-buckling paths (dotted and dashed curves) for  $v_0 = 0.01t$  and  $-0.01t$  coincide. This means that the D post-buckling *asymmetry* is exclusively due to the  $SM_u$  and  $SM_v$ .
- (ii) If only modes **1** and **5** are included, the  $v/t$  values are practically exact up to  $\sigma = 0.75\sigma_{cr}^D$  and  $\sigma = \sigma_{cr}^D$  ( $v_0 = 0.01t$  and  $-0.01t$ ) and progressively loses accuracy, particularly for  $v_0 = 0.01t$ : e.g., for  $v_0 = 0.01t$  and  $v/t = 3.0$ , one has  $\sigma_{ap} = 1.11\sigma_{cr}^D$ , instead of  $\sigma_{ex} = 0.98\sigma_{cr}^D$ . Including the remaining FM (**3** and **7**) only improves the solution slightly: e.g., again for  $v_0 = 0.01t$  and  $v/t = 3.0$ , one now has  $\sigma_{ap} = 1.09\sigma_{cr}^D$ .
- (iii) For  $v_0 = 0.01t$ , including all participating FM and  $SM_u$  (**1, 3, 5, 7, 15** and **23**) improves the accuracy significantly: for  $v/t = 3.0$ , one has now  $\sigma_{ap} = 1.02\sigma_{cr}^D$ ,

Table 3. Values of  $\varepsilon_\sigma$  and  $T_r$  for (a) LP (b) D ( $v < 0$ ) and (c) D ( $v > 0$ ) post-buckling.

(a)			(b)			(c)		
Modes	$T_r$	$\varepsilon_\sigma$	Modes	$T_r$	$\varepsilon_\sigma$	Modes	$T_r$	$\varepsilon_\sigma$
<b>1 + 7</b>	5.5	14.1	<b>1 + 5</b>	5.2	4.4	<b>1 + 5</b>	5.3	13.0
<b>+9 + 11</b>	12.6	7.0	<b>+3 + 7</b>	12	3.2	<b>+3 + 7</b>	12.1	11.6
<b>+26 + 28</b>	30.1	2.1	<b>+15 + 23</b>	24.9	2.0	<b>+15 + 23</b>	25.7	3.7
<b>+15 + 17</b>	45.1	0.8	<b>+26 + 28</b>	47.3	1.1	<b>+26 + 28</b>	48.6	1.0

only about 3% above the exact value. This shows that, for  $v_0/t > 0$ , accuracy can only be achieved if SM is included.

- (iv) For either  $v_0 = 0.01t$  or  $v_0 = -0.01t$ , including the 10 most relevant modes (**1, 3, 5, 7, 15, 17, 23, 26, 28** and **30**) yields virtually exact results (errors below 1%).

The computational efficiency (relation between accuracy and CPU time) of the GBT analyses can be assessed by examining the values given in Table 3 and plotted in Figs. 18(a) and (b). They show that the accuracy of the approximate results with the CPU time required to obtain them and consist of: (i) stress errors  $\varepsilon_\sigma = (\sigma_{ap}/\sigma_{ex} - 1)$ , for  $w/t = 1.5$  (LP) or  $v/t = 3.0$  (D), and (ii) “relative CPU times”  $T_r = CPU_{ap}/CPU_{ex}$ , where  $CPU_{ap}$  and  $CPU_{ex}$  are related to “approximate” and “exact” (all-mode) GBT analyses.

For the LP behavior, the computational efficiency is remarkable: including just six modes (**1 + 7 + 9 + 11 + 26 + 28**), one obtains an almost exact result ( $\varepsilon_\sigma = 2.1\%$ ) in about 30% of  $CPU_{ex}$ . For the D behavior with  $v < 0$ , the computational efficiency is even more remarkable: indeed, just two modes (**1 + 5**) lead to  $\sigma_{ap}$  with a 4.4% error in only 5% of  $CPU_{ex}$ . Finally, for the D behavior with  $v > 0$ , the efficiency is similar to the LP one: a six-mode analysis (**1 + 3 + 5 + 7 + 15 + 23**) yields an error of 3.7% in about 25% of  $CPU_{ex}$ . Finally, note that, all three cases, including eight modes, lead to virtually exact values ( $\varepsilon_\sigma < 1\%$ ) in less than half of  $CPU_{ex}$ .

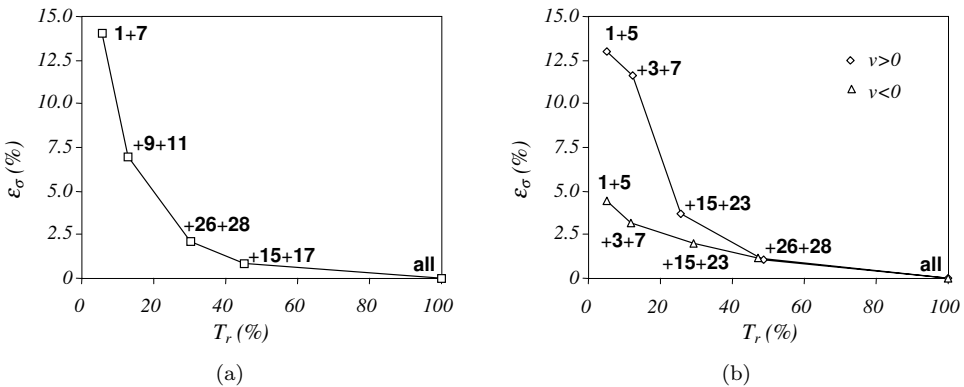


Fig. 18. Variation of  $\varepsilon_\sigma$  with  $T_r$  for (a) LP and (b) D ( $v < 0$  and  $v > 0$ ) post-buckling.

### 5.3. Z-section columns

Finally, consider Z-section columns with end support conditions, cross-section dimensions, node/FE discretizations and initial imperfections identical to the lipped channel columns analyzed before. Because both columns share the same LP and D stability behaviour, one again has:  $L_{LP} = 120$  mm,  $\sigma_{cr}^{LP} = 70.6$  MPa,  $L_D = 637$  mm and  $\sigma_{cr}^D = 31.8$  MPa. Since the Z-section is point-symmetric, the sign of  $v_0$  is now irrelevant (one flange-lip assembly “opens” and the other “closes”).

As expected, the GBT analyses show that the LP post-buckling paths of the C and Z-section columns coincide. Thus, the curve displayed in Fig. 14(a) also provides the LP post-buckling behavior of a Z-section column. On the other hand, the C and Z-section columns must exhibit distinct D post-buckling behaviors. Indeed, since the distortion patterns (i.e.,  $v$  signs) of the two flange-lip assemblies are *identical* in C-section columns and *opposite* in Z-section columns, one anticipates:

- (i) The D post-buckling paths associated to each of the Z-section column flange-lip assemblies to be different — the “closing” should display a stiffer behavior.
- (ii) The overall D post-critical strength of the Z-section column to lie between the post-critical strengths of the “opening” and “closing” C-section columns.

The results shown in Figs. 19(a) and (b), yielded by exact GBT analyses, confirm the above assertions. Figure 19(a) addresses the first one and displays the equilibrium paths related to the bottom and top lip (nodes **A** and **B**) displacements: the  $v_A/t$  (“closing” flange-lip) and  $v_B/t$  (“opening” flange-lip) curves split at  $\sigma \approx 1.03\sigma_{cr}^D$  and, naturally, the former exhibits a stiffer behavior. However, the

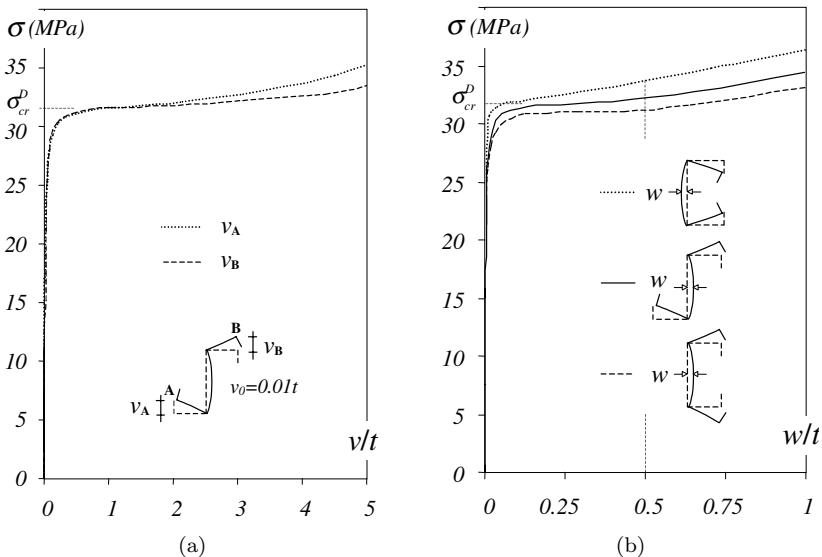


Fig. 19. Z-section column distortional post-buckling paths: (a)  $\sigma - v$  and (b)  $\sigma - w$ .

differences are now much smaller (recall that the paths concern different displacements of the *same* column).

A meaningful comparison between the overall D post-critical strength of the three columns (C-sections with  $v_0 = 0.01t$  and  $v_0 = -0.01t$  and Z-section with  $v_0 = \pm 0.01t$ ) must involve the equilibrium paths related to the mid-web flexural displacement  $w$  (since the D behavior of C and Z-section columns includes web flexure, one may compare three post-critical strengths concerning the *same displacement*). The paths are shown in Fig. 19(b) and, as predicted, the Z-section (solid) curve lies between the two C-section (dashed and dotted) curves: e.g., for  $w/t = 0.50$ , one has  $\sigma = 0.975\sigma_{cr}^D$  (C-section with  $v_0 = 0.01t$ ),  $\sigma = 1.014\sigma_{cr}^D$  (Z-section) and  $\sigma = 1.059\sigma_{cr}^D$  (C-section with  $v_0 = -0.01t$ ).

## 6. Conclusion

The paper presented the derivation of a geometrically nonlinear Generalized Beam Theory, intended to perform elastic post-buckling analyses of isotropic thin-walled members with open cross-sections (e.g., cold-formed steel profiles). This nonlinear GBT derivation involved the determination of linear and higher order cross-section mechanical properties (*cross-section analysis*) and the establishment of a system of member equilibrium equations (*member analysis*). The theory is able to handle several types of loading and can include arbitrary initial geometrical imperfections.

In order to derive this nonlinear GBT, it was necessary to go well beyond the available GBT, which is valid for small displacements only. Indeed, this derivation required considering two additional sets of deformation modes, namely shear and transverse extension modes, a fact rendering the cross-section analysis more complex.

After evaluating the cross-section modal mechanical properties and establishing the GBT system of member nonlinear equilibrium equations (one per deformation mode), a beam finite element was formulated to solve it, by means of an incremental-iterative technique employing Newton–Raphson method and arc-length control.

In order to validate and illustrate the application and capabilities of the nonlinear GBT, several numerical results were presented and discussed. These results dealt with the local-plate and distortional post-buckling behavior of uniformly compressed plates and lipped channel and Z-section columns. They consisted of:

- Identification and characterization of the relevant deformation modes.
- Post-buckling equilibrium paths, relating the values of the applied stress  $\sigma$  to the most appropriate cross-section displacements ( $w$  or  $v$ ).
- Graphs showing the evolution, along a given post-buckling path, of the GBT deformation mode participation in the member overall deformed configuration.

The equilibrium paths determined by means of the proposed nonlinear GBT were compared with values obtained from spline finite strip and finite element analyses. The comparisons showed that all-mode GBT analyses provide virtually exact results in all cases (errors below 1%). Moreover, it was shown that GBT

“approximate analyses”, which include just a selected subset of deformation modes, are very efficient: they yield rather accurate results with significantly less computational effort than the one required to perform “exact” (all-mode) analyses. Conventional numerical analyses do not offer such a possibility.

The column local-plate and distortional post-buckling analyses made it possible to:

- Conclude that accurate LP and D results require the inclusion of shear and transverse extension modes. These modes are more relevant in the D case, particularly for lipped channel columns with “opening” flange-lip assemblies.
- Show that the lipped channel column D post-buckling asymmetry, recently reported by Prola and Camotim,<sup>38</sup> is mostly due to shear deformation effects. Conventional numerical analyses could not provide such a clear explanation.

Finally, work is underway to apply the nonlinear GBT for the post-buckling analysis of cold-formed steel members affected by mode interaction phenomena. The GBT analyses are expected to shed new light on these phenomena and to provide an efficient tool to assess their relevance.

### Appendix

The components of the (i) linear stiffness matrices  $\mathbf{k}_1$ ,  $\mathbf{k}_2$ ,  $\mathbf{k}_3$  and  $\mathbf{k}_4$ , (ii) nonlinear stiffness matrix  $\mathbf{k}_5$  and (iii) force vectors  $\mathbf{f}_1$ ,  $\mathbf{f}_2$ ,  $\mathbf{f}_3$  and  $\mathbf{f}_4$  are given by

$$\mathbf{k}_1 = \frac{2}{L_e^3} \begin{bmatrix} 2L_e^2 & 3L_e & L_e^2 & -3L_e \\ & 6 & 3L_e & -6 \\ & & 2L_e^2 & -3L_e \\ \text{sym.} & & & 6 \end{bmatrix} \quad \mathbf{k}_2 = \frac{1}{30L_e} \begin{bmatrix} 4L_e^2 & 3L_e & -L_e^2 & -3L_e \\ & 36 & 3L_e & -36 \\ & & 4L_e^2 & -3L_e \\ \text{sym.} & & & 36 \end{bmatrix}$$

$$\mathbf{k}_3 = \frac{1}{30L_e} \begin{bmatrix} -4L_e^2 & -33L_e & L_e^2 & 3L_e \\ -3L_e & -36 & -3L_e & 36 \\ L_e^2 & -3L_e & -4L_e^2 & 33L_e \\ 3L_e & 36 & 3L_e & -36 \end{bmatrix} \quad \mathbf{k}_4 = \frac{L_e}{420} \begin{bmatrix} 4L_e^2 & 22L_e & -3L_e^2 & 13L_e \\ & 156 & -13L_e & 54 \\ & & 4L_e^2 & -22L_e \\ \text{sym.} & & & 156 \end{bmatrix}$$

$$\mathbf{k}_{5(1,1)} = \frac{1}{30}(\mathbf{d}_{j(3)} - 10\mathbf{d}_{j(1)}) + \frac{6}{30L_e}(\mathbf{d}_{j(2)} - \mathbf{d}_{j(4)})$$

$$\mathbf{k}_{5(1,2)} = -\mathbf{k}_{5(1,4)} = \frac{1}{5L_e}(\mathbf{d}_{j(1)} - 2\mathbf{d}_{j(3)}) + \frac{6}{5L_e^2}(\mathbf{d}_{j(4)} - \mathbf{d}_{j(2)})$$

$$\mathbf{k}_{5(1,3)} = \frac{1}{30}(\mathbf{d}_{j(1)} + 2\mathbf{d}_{j(3)}) + \frac{2}{5L_e}(\mathbf{d}_{j(4)} - \mathbf{d}_{j(2)})$$

$$\mathbf{k}_{5(2,1)} = -\mathbf{k}_{5(4,1)} = -\frac{2}{5L_e} \mathbf{d}_{j(1)} + \frac{3}{5L_e^2} (\mathbf{d}_{j(2)} - \mathbf{d}_{j(4)})$$

$$\mathbf{k}_{5(2,2)} = -\mathbf{k}_{5(2,4)} = -\mathbf{k}_{5(4,2)} = \mathbf{k}_{5(4,4)} = \frac{3}{5L_e^2} (\mathbf{d}_{j(1)} - \mathbf{d}_{j(3)})$$

$$\mathbf{k}_{5(2,3)} = -\mathbf{k}_{5(4,3)} = \frac{2}{5L_e} \mathbf{d}_{j(3)} + \frac{3}{5L_e^2} (\mathbf{d}_{j(4)} - \mathbf{d}_{j(2)})$$

$$\mathbf{k}_{5(3,1)} = -\frac{1}{30} (2\mathbf{d}_{j(1)} + \mathbf{d}_{j(3)}) + \frac{2}{5L_e} (\mathbf{d}_{j(2)} - \mathbf{d}_{j(4)})$$

$$\mathbf{k}_{5(3,2)} = -\mathbf{k}_{5(3,4)} = \frac{1}{5L_e} (2\mathbf{d}_{j(1)} - \mathbf{d}_{j(3)}) + \frac{6}{5L_e^2} (\mathbf{d}_{j(2)} - \mathbf{d}_{j(4)})$$

$$\mathbf{k}_{5(3,3)} = \frac{1}{30} (10\mathbf{d}_{j(3)} - \mathbf{d}_{j(1)}) + \frac{1}{5L_e} (\mathbf{d}_{j(4)} - \mathbf{d}_{j(2)})$$

$$\mathbf{f}_1 = \begin{Bmatrix} \frac{L_e^2}{12} \\ \frac{L_e}{2} \\ -\frac{L_e^2}{12} \\ \frac{L_e}{2} \end{Bmatrix} \quad \mathbf{f}_2 = \begin{Bmatrix} -1 \\ 0 \\ 1 \\ 0 \end{Bmatrix} \quad \mathbf{f}_3 = \begin{Bmatrix} 0 \\ -1 \\ 0 \\ 1 \end{Bmatrix} \quad \mathbf{f}_4 = \begin{Bmatrix} 0 \\ -q_x(0) \\ 0 \\ q_x(L_e) \end{Bmatrix}.$$

**References**

1. O. C. Zienkiewicz and R. L. Taylor, *The Finite Element Method*, 5th edn., Butterworth-Heinemann, Oxford, 2000.
2. M. A. Crisfield, *Nonlinear Finite Element Analysis of Solids and Structures Essentials*, Vol. 1, John Wiley & Sons, Chichester, 1991.
3. K. J. Bathe, *Finite Element Procedures in Engineering Analysis*, Prentice-Hall, Englewood-Cliffs, 1982.
4. K. J. Rasmussen, "Numerical simulation and computational models in coupled instabilities," *Coupled Instabilities in Metal Structures* (CIMS'96), eds. J. Rondal, D. Dubina e V. Gioncu, Imperial College Press, pp. 45–60, 1996.
5. Y. K. Cheung, *Finite Strip Method in Structural Analysis*, Pergamon Press, Oxford, 1976.
6. M. S. Cheung, W. Li and S. E. Chidiac, *Finite Strip Analysis of Bridges*, London, E & FN Spon, 1996.
7. J. S. Przemieniecki, "Finite element structural analysis of local instability," *AIAA J.* **11**(1), pp. 33–39, 1973.
8. R. J. Plank and W. H. Wittrick, "Buckling under combined loading of thin, flat-walled structures by a complex finite strip method," *Int. J. Num. Meth. Eng.* **8**(2), pp. 323–339, 1974.
9. G. J. Hancock, "Local, distortional and lateral buckling of *I*-beams," *J. Struct. Div. ASCE* **104**(11), pp. 1787–1798, 1978.

10. R. Schardt, "The generalized beam theory," *Instability and Plastic Collapse of Steel Structures*, Granada, London, pp. 469–475, 1983.
11. R. Schardt, *Verallgemeinerte Technische Biegetheorie (VTB)*, Berlin, Springer-Verlag, 1989 (in German).
12. S. C. Lau and G. J. Hancock, "Buckling of thin flat-walled structures by a spline finite strip method," *Thin-Walled Struct.* **4**(4), pp. 269–294, 1986.
13. Y. B. Kwon, *Post-Buckling Behaviour of Thin-Walled Channel Sections* PhD Thesis, School of Civil and Mining Engineering, University of Sydney, 1992.
14. L. C. Prola, *Local and Global Stability of Cold-Formed Steel Members* PhD Thesis, Civil Engineering Department, TU Lisbon, 2001 (in Portuguese).
15. M. Azhari, S. Hoshdar and M. A. Bradford, "On the use of bubble functions in the local buckling analysis of plate structures by the spline finite strip method," *Int. J. Num. Meth. Eng.* **48**(4), pp. 583–593, 2000.
16. R. H. Gallagher, "Finite element representations for thin shell instability analysis," *Buckling of Structures*, ed. B. Budiansky, Springer-Verlag, Berlin, pp. 40–51, 1974.
17. M. A. Crisfield, "Numerical analysis of structures," *Developments in Thin-Walled Structures*, eds. J. Rhodes *et al.*, Applied Science, pp. 235–284, 1981.
18. V. Ville de Goyet, "An advanced nonlinear spatial finite element," *Structural Stability and Design*, eds. S. Kitipornchai, G. Hancock and M. Bradford, Balkema, Rotterdam, pp. 249–254, 1995.
19. B. Young and J. Yan, "Finite element analysis and design of fixed-ended plain channel columns," *Finite Elem. Anal. Des.* **38**(6), pp. 549–566, 2002.
20. T. R. Graves Smith and S. Sridharan, "A finite strip method for the post-locally-buckled analysis of plate structures," *Int. J. Mech. Sci.* **20**(12), pp. 833–842, 1978.
21. G. J. Hancock, "Non-linear analysis of thin-walled sections in compression," *J. Struct. Div. ASCE* **107**(3), pp. 455–471, 1981.
22. S. Sridharan and T. R. Graves-Smith, "Post-buckling analyses with finite strips," *J. Eng. Mech. Div. ASCE* **107**(5), pp. 869–888, 1981.
23. P. Lengyel and A. R. Cusens, "A finite strip method for the geometrically nonlinear analysis of plate structures," *Int. J. Num. Meth. Eng.* **19**(3), pp. 331–340, 1983.
24. Z. G. Azizian and D. J. Dawe, "Geometrically non-linear analysis of thin-walled structures by finite strips," *Comput. Struct.* **21**(3), pp. 423–436, 1985.
25. Y. B. Kwon and G. J. Hancock, "A nonlinear elastic spline finite strip analysis for thin-walled sections," *Thin-Walled Struct.* **12**(4), pp. 295–319, 1991.
26. J. M. Davies, P. Leach and D. Heinz, "Second-order generalised beam theory," *J. Constr. Steel Res.* **31**(2–3), pp. 221–241, 1994.
27. J. M. Davies, "Recent research advances in cold-formed steel structures," *J. Constr. Steel Res.* **55**(1–3), pp. 267–288, 2000.
28. N. Silvestre and D. Camotim, "First order generalised beam theory for arbitrary orthotropic materials," *Thin-Walled Struct.* **40**(9), pp. 755–789, 2002.
29. N. Silvestre and D. Camotim, "Second order generalised beam theory for arbitrary orthotropic materials," *Thin-Walled Struct.* **40**(9), pp. 791–820, 2002.
30. N. Silvestre and D. Camotim, "GBT-based distortional buckling formulae for thin-walled channel columns and beams," *Recent Research and Developments in Cold-Formed Steel Design and Construction (Proc. 16th Int. Specialty Conf. — Orlando)*, pp. 68–83, 2002.
31. N. Silvestre and D. Camotim, "Shear deformable generalized beam theory" (submitted for publication).
32. R. M. Jones, *Mechanics of Composite Materials*, Taylor & Francis, Philadelphia 1999.
33. N. Silvestre and D. Camotim, "GBT buckling analysis of pultruded FRP lipped channel members," *Comput. Struct.* **81**(18–19), pp. 1889–1904, 2003.

34. N. Silvestre and D. Camotim, "GBT post-buckling analysis of cold-formed steel members," *Advances in Structures, Vol 1 (Proc. ASSCCA'03 — Sydney)*, eds. G. Hancock, M. Bradford, T. Wilkinson, B. Uy and K. Rasmussen, Balkema, Lisse, pp. 309–315, 2003.
35. Waterloo Maple Incorporation, *Maple 7*, Waterloo, Canada, 2001.
36. M. A. Crisfield, "A fast incremental/iterative solution procedure that handles snap-through," *Comput. Struct.* **13**(1–3), pp. 55–62, 1981.
37. Hibbit, Karlsson and Sorensen Inc., ABAQUS Standard (version 6.3), 2003.
38. L. C. Prola and D. Camotim, "On the distortional post-buckling behavior of cold-formed lipped channel steel columns," *Proc. SSRC Annual Stability Conf.*, Seattle, pp. 571–590, 2002.